

# Live-dead assay on unlabeled cells using phase imaging with computational specificity

Chenfei Hu <sup>1,2,8</sup>, Shenghua He<sup>3,8</sup>, Young Jae Lee <sup>2,4</sup>, Yuchen He <sup>1,2</sup>, Edward M. Kong<sup>2</sup>, Hua Li<sup>5,6,7</sup>, Mark A. Anastasio<sup>2,5</sup>✉ & Gabriel Popescu <sup>1,2,5</sup>✉

Existing approaches to evaluate cell viability involve cell staining with chemical reagents. However, the step of exogenous staining makes these methods undesirable for rapid, non-destructive, and long-term investigation. Here, we present an instantaneous viability assessment of unlabeled cells using phase imaging with computation specificity. This concept utilizes deep learning techniques to compute viability markers associated with the specimen measured by label-free quantitative phase imaging. Demonstrated on different live cell cultures, the proposed method reports approximately 95% accuracy in identifying live and dead cells. The evolution of the cell dry mass and nucleus area for the labeled and unlabeled populations reveal that the chemical reagents decrease viability. The nondestructive approach presented here may find a broad range of applications, from monitoring the production of biopharmaceuticals to assessing the effectiveness of cancer treatments.

<sup>1</sup>Electrical and Computer Engineering, University of Illinois at Urbana-Champaign, Urbana, IL, USA. <sup>2</sup>Beckman Institute for Advanced Science and Technology, University of Illinois at Urbana-Champaign, Urbana, IL, USA. <sup>3</sup>Department of Computer Science & Engineering, Washington University in St. Louis, St. Louis, MO, USA. <sup>4</sup>Neuroscience Program, University of Illinois at Urbana-Champaign, Urbana, IL, USA. <sup>5</sup>Department of Bioengineering, University of Illinois at Urbana-Champaign, Urbana, IL, USA. <sup>6</sup>Cancer Center at Illinois, Urbana, IL, USA. <sup>7</sup>Department of Radiation Oncology, Washington University in St. Louis, Saint Louis, MO, USA. <sup>8</sup>These authors contributed equally: Chenfei Hu, Shenghua He. ✉email: [maa@illinois.edu](mailto:maa@illinois.edu); [gpopescu@illinois.edu](mailto:gpopescu@illinois.edu)

Rapid and accurate estimation of the viability of biological cells is important for assessing the impact of drugs, physical or chemical stimulants, and other potential factors in cell function. The existing methods to evaluate cell viability commonly require mixing a population of cells with reagents to convert a substrate to a colored or fluorescent product<sup>1</sup>. For instance, using membrane integrity as an indicator, the live and dead cells can be separated by trypan blue exclusion assay, where only nonviable cells are stained and appear as a distinctive blue color under a microscope<sup>2,3</sup>. MTT and XTT assay estimate the viability of a cell population by measuring the optical absorbance caused by formazan concentration due to alteration in mitochondrial activity<sup>4–6</sup>. Starting in the 1970s, fluorescence imaging has developed as a more accurate, faster, and reliable method to determine cell viability<sup>7–10</sup>. Similar to the principle of trypan blue test, this method identifies individual nonviable cells by using fluorescent reagents only taken up by cells that lost their membrane permeability barrier. Unfortunately, the step of exogenous labeling generally requires some incubation time for optimal staining intensity, making all these methods difficult for quick evaluation. Importantly, the toxicity introduced by stains eventually kills the cells and, thus, prevents the long-term investigation.

Quantitative phase imaging (QPI) is a label-free modality that has gained significant interest due to its broad range of potential biomedical applications<sup>11,12</sup>. QPI measures the optical phase delay across the specimen as an intrinsic contrast mechanism, and thus, allows visualizing transparent specimen (i.e., cells and thin tissue slices) with nanometer scale sensitivity, which makes this modality particularly useful for nondestructive investigations of cell dynamics (i.e. growth, proliferation, and mass transport) in both 2D and 3D<sup>13–18</sup>. In addition, the optical phase delay is linearly related to the non-aqueous content in cells (referred to as dry mass), which directly yields biophysical properties of the sample of interest<sup>19–22</sup>. More recently, with the concomitant advances in deep learning, we have witnessed exciting avenues for label-free imaging. In 2018, Google presented “in silico labeling”, a deep learning based approach that can predict fluorescent labels from

transmitted-light (bright field and phase contrast) images of unlabeled samples<sup>23</sup>. Around the same time, researchers from the Allen Institute showed that individual subcellular structures such as DNA, cell membrane, and mitochondria can be obtained computationally from bright-field images<sup>24</sup>. Because a QPI map quantitatively encodes structure and biophysical information, it is possible to apply deep learning techniques to extract subcellular structures<sup>25,26</sup>, perform signal reconstruction<sup>27,28</sup>, correct image artifacts<sup>29,30</sup>, convert QPI data into virtually stained or fluorescent images<sup>31,32</sup>, and diagnose and classify various specimens<sup>33,34</sup>.

In this article, we demonstrate that rapid viability assay can be conducted in a label-free manner using spatial light interference microscopy (SLIM)<sup>35,36</sup>, a highly sensitive QPI method, and deep learning. We apply the concept of phase imaging with computational specificity (PICS) to digitally stain for the live and dead markers. Demonstrated on live adherent HeLa and CHO cell cultures, we predict the viability of individual cells measured with SLIM by using a joint EfficientNet<sup>37</sup> and transfer learning<sup>38</sup> strategy. Using the standard fluorescent viability imaging as ground truth, the trained neural network classifies the viable state of individual cell with 95% accuracy. Furthermore, by tracking the cell morphology over time, unstained HeLa cells show significantly higher viability compared to the cells stained with viability reagents. These findings suggest that the PICS method enables rapid, nondestructive, and unbiased cell viability assessment, potentially valuable to a broad range of biomedical problems, from drug testing to the production of biopharmaceuticals.

## Results

The procedure of image acquisition is summarized in Fig. 1. We employed spatial light interference microscopy (SLIM)<sup>35</sup> to measure the quantitative phase map of cells in vitro. The system is built by attaching a SLIM module (CellVista SLIM Pro, Phi Optics, Inc.) to the output port of an existing phase-contrast microscope (Fig. 1a). By modulating the optical phase delay between the incident and the scattered field, a quantitative phase map is retrieved from four intensity images via phase-shifting

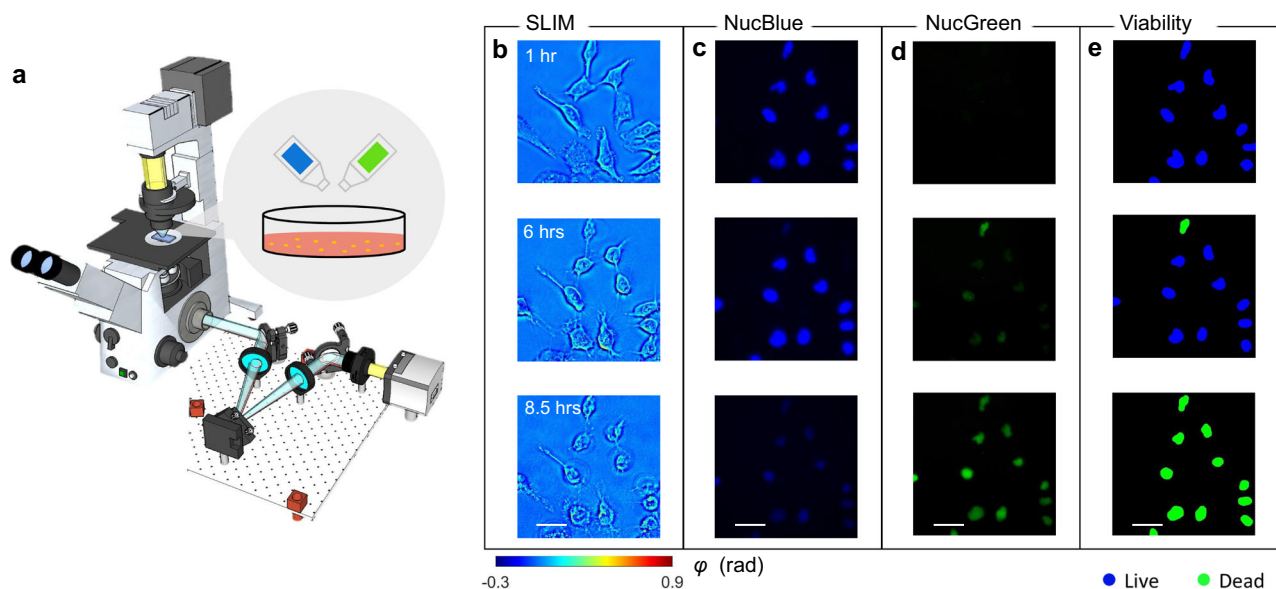


**Fig. 1** Schematic of the imaging system and representative results. **a** CellVista SLIM Pro microscope (Phi Optics, Inc.) consists of an existing phase contrast microscope and an external module attached to the output port. By switching between transmission and reflection excitation, both SLIM and co-localized fluorescence images can be recorded via the same optical path. Before time-lapse imaging started, fluorescence viability reagents were mixed with the cell culture. **b** Representative SLIM measurements of HeLa cell at 1, 6, and 8.5 h after staining. The experiment is repeated 4 times. **c** NucBlue fluorescent signals of the live viability reagent. **d** NucGreen fluorescent signals of the dead viability reagents measured. **e** Viability states of the individual cells. Source data are provided as a Source Data file. Scale bars: 50  $\mu\text{m}$  in space.

interferometry<sup>39</sup>. SLIM employs broadband LED as an illumination source and common-path imaging architecture, which yields sub-nanometer sensitivity to optical pathlength changes and high temporal stability<sup>39,40</sup>. By switching to epi-illumination, the optical path of SLIM is also used to record the fluorescent signals over the same field of view. Detailed information about the microscope configuration can be found in Methods.

To demonstrate the feasibility of the proposed method, we imaged and analyzed live cell cultures. Before imaging, 40  $\mu$ L of each cell-viability-assay reagent (ReadyProbes Cells Viability Imaging Kit, Thermofisher) was added into 1 ml growth media, and the cells were then incubated for approximately 15 min to achieve optimal staining intensity. The viability-assay kit contains two fluorescently labeled reagents: NucBlue (the “live” reagent) combines with the nuclei of all cells and can be imaged with a DAPI fluorescent filter set, and NucGreen (the “dead” reagent) stains the nuclei of cells with compromised membrane integrity, which is imaged with a FITC filter set. In this assay, live cells produce a blue-fluorescent signal; dead cells emit both green and blue fluorescence; The procedure of cell culture preparation can be found in Methods.

After staining, the sample was transferred to the microscope stage, and measured by SLIM and epi-fluorescence microscopy. In order to generate a heterogeneous cell distribution that shifts from predominantly alive to mostly dead cells, the imaging was performed under room conditions, such that the low-temperature and imbalanced pH level in the media would adversely injure the cells and eventually cause necrosis. Recording one measurement every 30 or 60 min, the entire imaging process lasted for approximately 10 h. We repeated this experiment four times to capture the variability among different batches. Figure 1b shows the SLIM images of HeLa cells measured at  $t = 1$  h, 6, and 8.5 h, respectively, and the corresponding fluorescent measurements are shown in Fig. 1c, d. The results in Fig. 1 show that the adverse environmental condition continues injuring the cell, where blebbing and membrane disruption could be observed during cell death. Our QPI measurements agree with the results reported in previous literature<sup>41</sup>. On the other hand, these morphological alterations are correlated with the changes in fluorescence signals, where the intensity of NucGreen (“dead” fluorescent channel) continuously increases, as cells transit to dead states. By comparing the relative intensity between NucGreen and NucBlue signals, semantic segmentation maps are generated to label individual cell as either live or dead, as shown in Fig. 1e. The procedure of generating the semantic maps can be found in Supplemental Note 1. All collected image sequences were combined to form a dataset for PICS training and testing, where each sequence is a time-lapse recording of cells from live to dead states. Then we randomly split the sequences with a ratio of approximately 6:1:1, to obtain training, validation, and testing dataset, respectively. Instead of splitting by frame, we generated a training dataset by dividing image sequences to ensure fair generalization. In addition, we combined data across all measurements to take underrepresented cellular activities into account, which makes the proposed method generalizable.

**Deep neural network architecture, training, validation, and testing.** With fluorescence-based semantic maps as ground truth, a deep neural network was trained to assign “live”, “dead”, or background labels to pixels in the input SLIM images. We employed a U-Net based on EfficientNet (E-U-Net)<sup>37</sup>, with its architecture shown in Fig. 2a. Compared to conventional U-Nets, the E-U-Net uses EfficientNet<sup>37</sup>, a powerful network of relatively lower complexity, as the encoding part. This architecture allows for learning an efficient and accurate end-to-end segmentation

model, while avoiding training a very complex network. The network was trained using a transfer learning strategy<sup>38</sup> with a finite training set. At first, the EfficientNet of E-U-Net (the encoding part) was pre-trained for image classification on a publicly available dataset ImageNet<sup>42</sup>. The entire E-U-Net was then further fine-tuned for a semantic segmentation task by using labeled SLIM images from the training and validation set.

The network training was performed by updating the weights of parameters in the E-U-Net using an Adam optimizer<sup>43</sup> to minimize a loss function that is computed in the training set. More details about the EfficientNet module and loss function can be found in the Methods and Supplemental Note 2. The network was trained for 100 epochs. At the end of each epoch, the loss function related to the being-trained network was evaluated, and the weights that yielded the lowest loss on the validation set were selected for the E-U-Net model. Figure 2d shows training and validation loss vs. the number of epochs, using 899 and 199 labeled images as training and validation datasets. The Methods section and Fig. 2a–c present more details about the E-U-Net architecture and network training.

To demonstrate the performance of phase imaging with computational specificity (PICS) as a label-free live/dead assay, we applied the trained network to 200 SLIM images not used in training and validation. Figure 3a shows the three representative testing phase maps, whereas corresponding ground truth and PICS prediction are shown in Fig. 3b, c, respectively. This direct comparison indicates that PICS successfully classifies the cell states. We found that, most often, the incorrect predictions were caused by cells located at the boundary of FOV, where only a portion of their cell bodies was measured by SLIM. In addition, PICS may fail when cells become detached from the well plates. In this situation, the suspended cells appear out of focus, which gives rise to inaccurate prediction. As reported in previous publications, the conventional deep learning evaluation metrics focus on assessing pixel-wise segmentation accuracy, which overlooks some biologically relevant instances<sup>44</sup>. Here, we adopted an object-based evaluation metric, which relies on comparing the dominant semantic label between the predicted cell nuclei and the ground truth for individual nuclei. The confusion matrix and the corresponding evaluation (e.g., precision, recall, and F1-score) are shown in Table 1. A comparison with standard pixel-wise evaluation and procedure of object-based evaluation are included in Supplemental Note 3. The entries of the confusion matrix are normalized with respect to the number of cells in each category. Using the average F1 score across all categories as an indicator of the overall performance, this PICS strategy reports a 96.7% confidence in distinguishing individual live and dead HeLa cells.

**PICS on CHO cells.** Chinese hamster ovary (CHO) cells are often used for recombinant protein production, and it received U.S. FDA approval for bio-therapeutic protein production. Here, we demonstrate that our label-free viability assay approach is applicable to other cell lines of interest in pharmaceutical applications. CHO cells were plated on a glass-bottom 6-well plate for optimal confluency. In addition to NucBlue/NucGreen staining, 1  $\mu$ M of staurosporine (apoptotic inducing reagent) solution was added to the culture medium. This potent reagent permeates the cell membrane and disrupts protein kinase, cAMP, and leads to apoptosis in 4–6 h. The cells were then measured by SLIM and epi-fluorescence microscopy. The cells were maintained in regular incubation conditions (37 °C and 5% concentration of CO<sub>2</sub>) throughout the experiment. In addition, we verified that the cells were not affected by necrosis and lytic cell death (see Supplemental Note 4). After image acquisition, E-U-Net (EfficientNet-B7) training was immediately followed. In the training process,

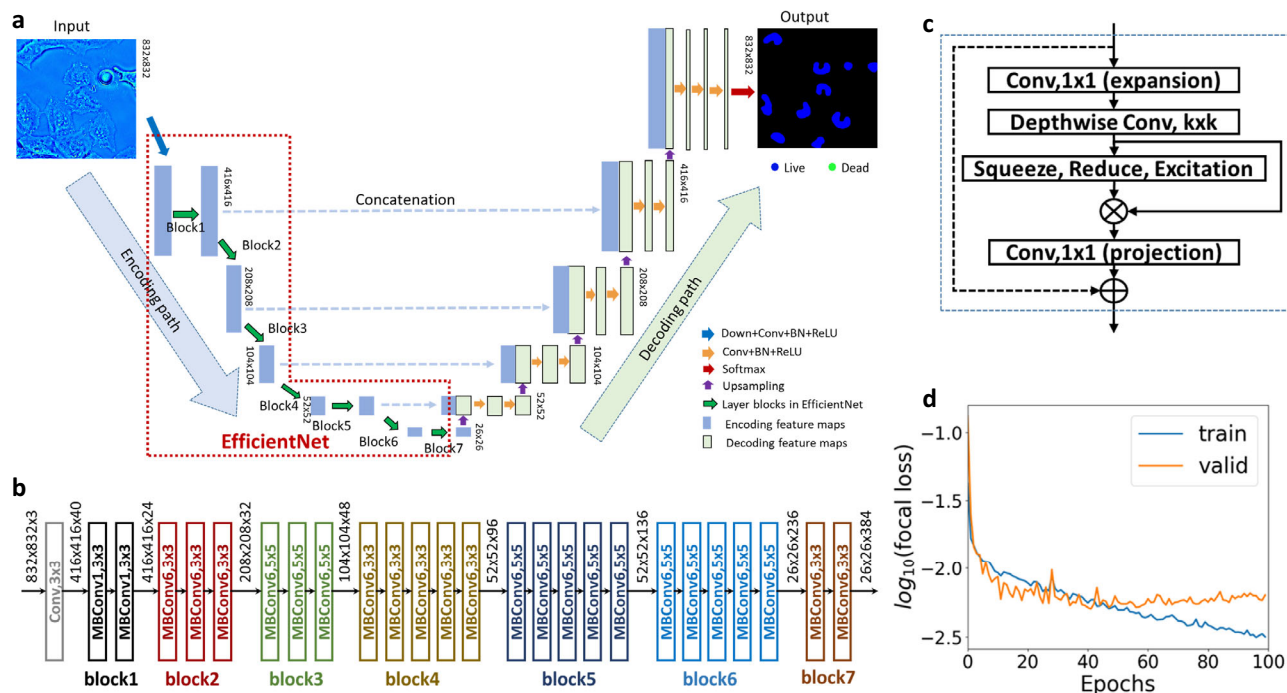


**Fig. 2 Principle of E-U-Net training.** **a** The E-U-Net architecture includes an EfficientNet as the encoding path and five stages of decoding. The E-U-Net includes a Down+Conv+BN+ReLU block and 7 other blocks. The Down-Conv-BN-ReLU block represents a chain of down-sampling layer, convolutional layer, batch normalization layer, and ReLU layer. Similarly, the Conv+BN+ReLU is a chain of convolutional layer, batch normalization layer, and ReLU layer. **b** The network architecture of EfficientNet-B3. Different blocks are marked in different colors. They correspond to the layer blocks of EfficientNet in **a**. **c** The major layers inside the MBCConvX module. X = 1 and X = 6 indicate the ReLU and ReLU6 are used in the module, respectively. The skip connection between the input and output of the module is not used in the first MBCConvX module in each layer block. **d** Training and validation loss vs epochs plotted in the log scale.

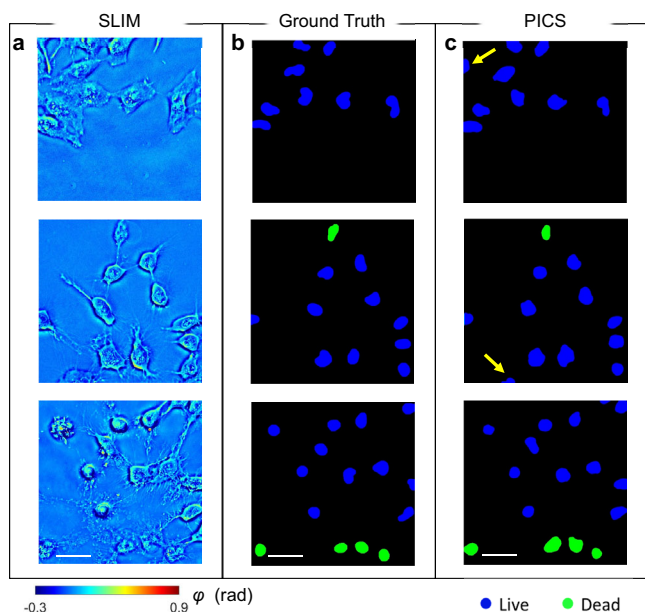


**Fig. 3 Results of E-U-Net on testing dataset.** **a** representative SLIM measurements of HeLa cells not used during training. **b** The ground truth for viability of frames corresponding to **a**. **c** The PICS prediction shows high level accuracy in segmenting the nuclear regions and inferring viability states. The arrows indicate the inconsistency between ground truth and PICS prediction caused by the cells located at the edge of the FOV are subject to inference error. The images are randomly selected from a combined dataset across 4 imaging experiments. Source data are provided as a Source Data file. Scale bars: 50  $\mu$ m in space.

**Table 1 Evaluation of the E-U-Net performance.**

		Ground Truth	
		Live (n = 1973)	Dead (n = 246)
PICS	Live	98.8%	2.4%
	Dead	1.2%	97.6%
Evaluation	Precision	99.6%	91.2%
	Recall	98.8%	97.6%
	F1 Score	99.1%	94.3%

An object-based accuracy metric is used to estimate the deep learning prediction by comparing the dominant semantic label of HeLa cell nuclei with the ground truth. The entries of the confusion are normalized with respect to number of cells in each class.

1536 labeled SLIM images and 288 labeled SLIM images were used for network training and validation, respectively. The structure of EfficientNet-B7, training, and validation loss can be found in Fig. S3a, b, respectively. The trained E-U-net was finally applied to 288 unseen testing images to test the performance of dead/viability assay. The procedure of imaging, ground truth generation, and training was consistent with the previous experiments.

Figure 4a shows the time-lapse SLIM image of CHO cells measured at t = 0, 2, and 10 h after adding apoptosis reagent, and the corresponding viability map determined by fluorescence signal and PICS are plotted in Fig. 4b, c, respectively. In contrast to necrosis, the cell bodies became gradually fragmented during apoptosis. The visual comparison in Fig. 4 suggests that PICS yields good performance in extracting cell nucleus and predicting their viable state. Running an evaluation on individual cells, as

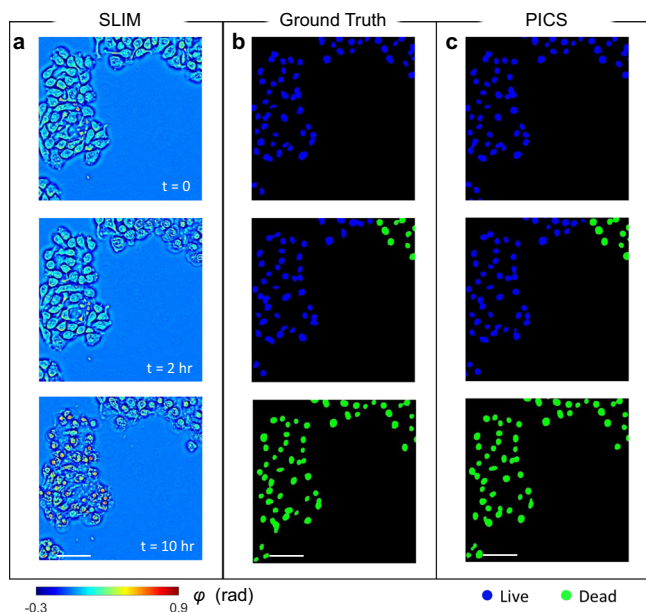


**Fig. 4 Results of PICS on adherent CHO cells.** **a** Time-lapse SLIM measurement of CHO cells measured at  $t = 0, 2,$  and  $10$  h. The data was not used in training or validation. **b** The ground truth for viability of frames corresponding to **a**. **c** The PICS prediction shows high level accuracy in segmenting the nuclear regions and inferring viability states. The images are randomly selected from a combined dataset across 4 imaging experiments. Scale bars:  $50 \mu\text{m}$  in space.

**Table 2 Evaluation of the E-U-Net performance on CHO with apoptosis reagents.**

		Ground truth	
		Live ( $n = 2071$ )	Dead ( $n = 6328$ )
PICS	Live	90.1%	1.7%
	Dead	9.9%	98.3%
Evaluation	Precision	94.6%	96.8%
	Recall	90.1%	98.3%
	F1 Score	92.3%	97.5%

The trained network yields high confidence in identifying live or apoptotic CHO cells. The entries of the confusion are normalized with respect to number of cells in each class.

shown in Table 2, the network gives an average F-1 score of 94.9%. Again, the inaccurate prediction is mainly caused by cells at the boundary of the FOV. We also found rare cases where cells show features of cells death at early stage<sup>45–47</sup>, but it was identified as live by traditional fluorometric evaluation (for example, see Fig. S5 in the Supplemental Information). Furthermore, because most of the cells stay adherent, the PICS accuracy was not affected by cell confluence. The evaluation metrics at different confluence levels are included in the Supplemental Note 4.

**PICS on unlabeled HeLa cells.** Performing viability assay on unlabeled cells essentially circumvents the cell injury effect caused by exogenous staining and produces an unbiased evaluation. To demonstrate this feature on a different cell type, a fresh HeLa cell culture was prepared in a 6-well plate, transferred to the microscope stage, and maintained under room conditions. Half of the wells were mixed with viability assay reagents, where the viability

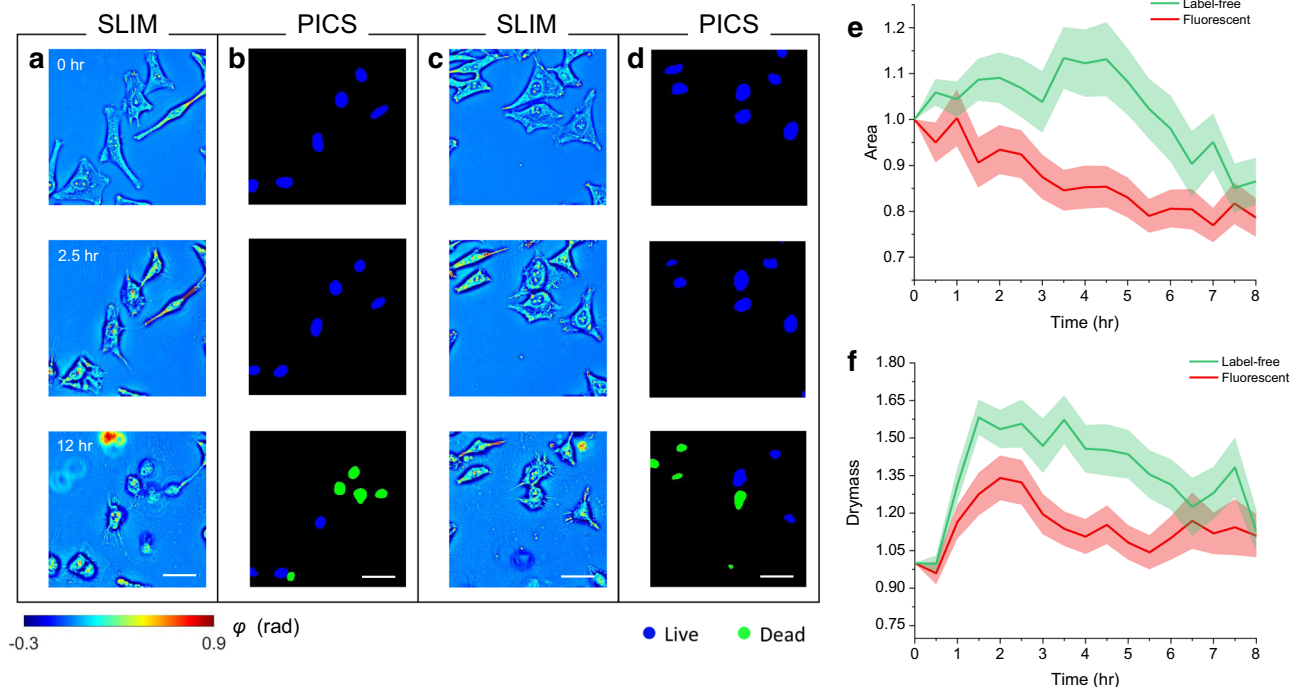
was determined by both PICS and fluorescence imaging. The remaining wells did not contain reagents, such that the viability of these cells was only evaluated by PICS. The procedure of cell preparation, staining, and microscope settings were consistent with the previous experiments. We took measurements every 30 min, and the entire experiment lasted for 12 h.

Figure 5a and c shows SLIM images of HeLa cells with and without fluorescent reagents at  $t = 0, 2.5,$  and  $12$  h, respectively, whereas the resulting PICS predictions are shown in Fig. 5b and d. Supplemental Video 1 shows a time-lapse SLIM measurement, PICS prediction, and standard live-dead assay based on fluorescent measurements. Supplemental Video 2 shows HeLa cells without reagents. As expected, the PICS method depicts the transition from live to dead state. In addition, the visual comparison from Fig. 5a–d suggests that HeLa cells with viability stains in the media appear smaller in size, and more rapidly enter the injured state, as compared to their label-free counterparts. Using TrackMate<sup>48</sup>, an ImageJ plugin, we were able to extract the trajectory of individual cells and track their morphology over time. As a result, the cell nucleus, area, and dry mass at each moment in time can be obtained by integrating the pixel value over the segmented area in the PICS prediction and SLIM image, respectively. We successfully tracked 57 labeled and 34 unlabeled HeLa cells. Figure 5e, f shows the area and dry mass change (mean  $\pm$  standard error), where the values are normalized with respect to the one at  $t = 0$ . Our results of tracking agree with the physiological description<sup>49,50</sup>, and are consistent with previously reported experimental validations<sup>46,51</sup>. However, the short swelling time in the reagent-treated cells suggests the toxicity of the chemical compounds would potentially accelerate the pace of cell death. Running two-sample t-tests, we found a significant difference in cell nuclear areas between the labeled and unlabeled cells, during the interval  $t = 2$  and  $t = 7$  h ( $p < 0.05$ ). Similarly, cell dry mass showed significant differences between the two groups during the time interval  $t = 2$  and  $t = 5$  h ( $p < 0.05$ ). In this study, we focus on optimizing the PICS performance in classifying live/dead markers at the cellular level. At the pixel level, the trained network can reveal the cell shape change, but its performance in capturing the nucleus shape and area is limited, which makes the current approach subject to segmentation error. This is largely due to the low contrast between the nucleus boundary and cytoplasm in injured cells.

Although the effect of the fluorescent dye itself on the optical properties of the cell at the imaging wavelength is negligible<sup>52–55</sup>, training on images of tagged cells may potentially alter the cell death mechanism and introduce bias when optimizing the E-U-Net. To investigate this potential concern, we performed a set of experiments where the unlabeled cells were imaged first by SLIM, then tagged and imaged by fluorescence for ground truth. As described in Supplemental Note 4, we found that the performance of PICS, in this case, was consistent with the results shown in Figs. 3 and 4, where SLIM was applied to tagged cells. The data indicated that the live and dead cells were classified with 99% and 97% sensitivity, respectively, suggesting that the proposed live-dead assay method can be used efficiently on cells that were never labeled. Of course, SLIM imaging of already stained cells, followed by fluorescence imaging, is a more practical workflow, as the input-ground truth image pairs can be collected continuously. On the other hand, training on unlabeled cells allows us to achieve the true label-free assay which is most valuable in applications.

## Discussion

We demonstrated PICS as a method for high-speed, label-free, unbiased viability assessment of adherent cells. This approach utilizes quantitative phase imaging to record high-resolution



**Fig. 5 Viability of HeLa cells with and without reagent stains. a.** SLIM images of cells recorded at 0, 2.5 and 12 h after staining. **b.** The PICS prediction associated with the frames in **a.** **c.** SLIM images of unstained HeLa cells measured at same time points as **a.** **d.** The corresponding PICS prediction associated with the frames in **c.** **e.** Relative cell nuclear area change of tracked cells. The central line represents the average, and the shaded region indicates the standard error. **f.** Relative cell nucleus dry mass change. The central line represents the average, and the shaded region indicates the standard error. Source data are provided as a Source Data file. Scale bars: 50  $\mu\text{m}$  in space.

morphological structures of unstained cells, combined with deep learning techniques to extract intrinsic viability markers. Tested on HeLa and CHO adherent cultures, our optimized E-U-Net method reports outstanding accuracy of 96.7% and 94.9% in segmenting the cell nuclei and classifying their viability state. In Supplemental Note 5, we compared the E-U-Net accuracy with the outcomes from other networks or training strategies. By integrating the trained network on NVIDIA graphic processing units, the proposed label-free method enables real-time acquisition and viability prediction (see Supplemental Video 3 for a demonstration). One SLIM measurement and deep learning prediction take  $\sim 100$  ms, which is approximately 8 times faster than the acquisition time required for fluorescence imaging with the same camera. Of course, the cell staining process itself takes time, approximately 15 min in our case. The real-time in situ feedback is particularly useful in investigating viability state and growth kinetics in cells, bacteria, and samples in vivo over extended periods of time<sup>56–59</sup>. In addition, results suggest that PICS rules out the adverse effect on cell function caused by the exogenous staining, which is beneficial for the unbiased assessment of cellular activity over a long time (e.g., many days). Of course, this approach can be applied to other cell types and cell death mechanisms.

Prior studies typically tracked QPI parameters associated with individual cells over time to identify morphological features correlated with cell death<sup>45,46,51</sup>. In contrast, our approach provides a real-time classification of cells based on single frames, which is a much more challenging and rewarding task. Compared to these previous studies, our PICS method avoids intermediate steps of feature extraction, manual annotation, and separate algorithms for training & cell classification. We employ a single DNN architecture with direct QPI measurement as input, and the prediction accuracy is significantly improved over the previously reported data<sup>47</sup>. The labels output by the network can be used to create binary masks,

which in turn yield dry mass information from the input data. The accuracy of these measurements depends on the segmentation process. Thus, we anticipate that future studies will optimize further the segmentation algorithms to yield high-accuracy dry mass measurements over long periods of time.

Label-free imaging methods are valuable for studying biological samples without destructive fixation or staining. For example, by employing infrared spectroscopy, the bond-selective transient phase imaging measures molecular information associated with lipid droplets and nucleic acids<sup>60</sup>. In addition, harmonic optical tomography can be integrated into an existing QPI system to report specifically on non-centrosymmetric structures<sup>61</sup>. These additional chemical signatures would potentially enhance effective learning and produce more biophysical information. We anticipate that the PICS method will provide high-throughput cell screening for a variety of applications, ranging from basic research to therapeutic development and protein production in cell reactors<sup>11</sup>. Because SLIM can be implemented as an upgrade module onto an existing microscope and integrates seamlessly with fluorescence, one can implement this label-free viability assay with ease.

## Methods

**Cell preparation.** HeLa cervical cancer cells (ATCC CCL-2<sup>TM</sup>) and Chinese hamster ovary (CHO-K1 ATCC CCL-61<sup>TM</sup>) cells were purchased from ATCC and kept frozen in liquid nitrogen. Before the experiments, we thawed and cultured the cells into a T75 flask in Dulbecco's Modified Eagle Medium (DMEM with low glucose) containing 10% fetal bovine serum (FBS) and incubated in 37 °C with 5% CO<sub>2</sub>. As the cells reach 70% confluence, the flask was washed thoroughly with phosphate-buffered saline (PBS) and trypsinized with 3 mL of 0.25% (w/v) Trypsin EDTA for three minutes. When the cell starts to detach, the cells were suspended in 5 mL DMEM and passaged onto a glass-bottom 6 well plate to grow. To evaluate the effect of confluency on PICS performance, CHO cells were plated in three different confluency levels: high (60,000 cells), medium (30,000 cells), and low (15,000 cells). HeLa and CHO cells were then imaged after two days.

**SLIM imaging.** The SLIM optical setup is shown in Fig. 1a. In brief, the microscope is built upon an inverted phase-contrast microscope with a SLIM module (CellVista SLIM Pro; Phi Optics) attached to the output port. Inside the module, a spatial light modulator (Meadowlark Optics) is placed at the system pupil plane via a Fourier transform lens to constantly modulate the phase delay between the scattered and incident light. By recording four intensity images with phase shifts of  $0, \pi/2, \pi,$  and  $3\pi/2$ , a quantitative phase map,  $\phi$ , can be computed by combining the 4 acquired frames in real-time.

For both SLIM and fluorescence imaging, cultured cells were measured by a 40 $\times$  objective, and the images were recorded by a CMOS camera (ORCA-Flash 4.0; Hamamatsu) with a pixel size of 6.5  $\mu\text{m}$ . For each sample, we randomly selected a cellular region approximately  $800 \times 800 \mu\text{m}^2$  to be measured by SLIM and fluorescence microscopy (NucBlue and NucGreen). The acquisition time of each SLIM and fluorescent measurements are 50 ms and 400 ms, respectively, and the scanning across all 6 wells takes roughly 4.3 min, where the delay is caused by mechanical translation of the motorized stage. For deep learning training and predicting, the recorded SLIM images were downsampled by a factor of 2. This step saves computational cost and does not sacrifice information content. We would like to point out that the acquisition of the fluorescence data is needed only for the training stage. For real-time interference, our acquisition is up to 15 frames per second for SLIM images, while the inference takes place in parallel.

**E-U-Net architecture.** The E-U-Net is a U-Net-like fully convolutional neural network that performs an efficient end-to-end mapping from SLIM images to the corresponding probability maps, from which the desired segmentation maps are determined by the use of a softmax decision rule. Different from conventional U-Nets, the E-U-Net uses a more efficient network architecture, EfficientNet<sup>37</sup>, for feature extraction in the encoding path. Here, EfficientNets refers to a family of deep convolutional neural networks that possess a powerful capacity of feature extraction but require much fewer network parameters compared to other state-of-the-art network architectures, such as VGG-Net, ResNet, Mask R-CNN, etc. The EfficientNet family includes eight network architectures, EfficientNet-B0 to EfficientNet-B7, with an increasing network complexity. EfficientNet-B3 and EfficientNet-B7 were selected for training E-U-Net on HeLa cell images and CHO cell images, respectively, considering they yield the most accurate segmentation performance on the validation set among all the eight EfficientNets. See Supplemental Note 2 and Fig. 2b, c for more details about the EfficientNet-B3 and EfficientNet-B7.

**Loss function and network training.** Given a set of  $B$  training images of  $M \times N$  pixels and their corresponding ground truth semantic segmentation maps, loss function used for network training is defined as the combination of focal loss<sup>62</sup> and dice loss<sup>63</sup>:

$$L_{\text{Focal\_loss}} = -\frac{1}{B} \sum_{i=1}^B \frac{1}{MN} \sum_{x \in \Omega} [1 - y_i(x)^T p_i(x)]^\gamma y_i(x)^T \log_2 p_i(x), \quad (1)$$

$$L_{\text{Dice\_loss}} = 1 - \frac{1}{3} \sum_{c=0}^2 \frac{2TP_c}{2TP_c + FP_c + FN_c} \quad (2)$$

$$L_{\text{combined}} = \alpha L_{\text{Focal\_loss}} + \beta L_{\text{Dice\_loss}} \quad (3)$$

In the focal loss  $L_{\text{Focal\_loss}}$   $\Omega = \{(1, 1), (1, 2), \dots, (M, N)\}$  is the set of spatial locations of all the pixels in a label map.  $y_i(x) \in \{[1, 0, 0]^T, [0, 1, 0]^T, [0, 0, 1]^T\}$  represents the ground-truth label of the pixel  $x$  related to the  $i^{\text{th}}$  training sample, and the three one-hot vectors correspond to the live, dead and, background classes, respectively. Accordingly, the probability vector  $\mathbf{P}_i(x) \in \mathbb{R}^3$  represents the corresponding predicted probabilities belonging to the three classes.

$[1 - y_i(x)^T p_i(x)]^\gamma$  is a classification error-related weight that reduces the relative cross-entropy  $y_i(x)^T \log_2 p_i(x)$  for well-classified pixels, putting more focus on hard, misclassified pixels. In this study,  $\gamma$  was set to be the default value of 2 as suggested in Ref. 62. As the dice loss  $L_{\text{Dice\_loss}}$ , the  $TP_c$ ,  $FP_c$ , and  $FN_c$  are the number of true positives, that of false positives, and that of false negatives, respectively, related to all pixels of viability class  $c \in \{0, 1, 2\}$  in the  $B$  images. Here,  $c = 0, 1,$  and  $2$  correspond to the live, dead, and background classes, respectively. In the combined loss function,  $\alpha, \beta \in \{0, 1\}$  are two indicators that control whether to use focal loss and dice loss in the training process, respectively. In this study,  $\alpha$  and  $\beta$  were set to  $[1, 0]$  and  $[1, 1]$  for training the E-U-Nets on the HeLa cell dataset and CHO cell dataset, respectively. The choices of  $[\alpha, \beta]$  were determined by the segmentation performance of the trained E-U-Net on the validation set.

The E-U-Net was trained with randomly cropped patches of  $512 \times 512$  pixels drawn from the training set by minimizing the loss function defined above with an Adam optimizer<sup>43</sup>. In regard to Adam optimizer, the exponential decay rates for 1<sup>st</sup> and 2<sup>nd</sup> moment estimates were set to 0.9 and 0.999, respectively; a small constant  $\epsilon$  for numerical stability was set to  $10^{-7}$ . The batch sizes were set to 14 and 4 for training the E-U-nets on the HeLa cell images and CHO cell images, respectively. The learning rate was initially set to  $5 \times 10^{-4}$ . At the end of each epoch, the loss of a being-trained E-U-Net was computed on the whole validation set. When the validation loss did not decrease for 10 training epochs, the learning rate was multiplied by a factor of 0.8. This validation loss-aware learning rate decaying strategy benefits for mitigating the overfitting issue that commonly occurs in deep neural network training. Furthermore, data augmentation techniques, such as random cropping, flipping, shifting, and random noise and brightness adding, etc.,

were employed to augment training samples on the fly for further reducing the overfitting risk. The E-U-Net was trained for 100 epochs. The parameter weights that yield the lowest validation loss were selected and subsequently used for model testing and further model investigation.

The E-U-Net was implemented using the Python programming language with libraries including Python 3.6 and Tensorflow 1.14. The model training, validation, and testing were performed on an NVIDIA Tesla V100 GPU of 32 GB VRAM.

**Reporting summary.** Further information on research design is available in the Nature Research Reporting Summary linked to this article.

## Data availability

Source data producing the graphs in the article are provided with this paper. In addition, an example set of the SLIM images and corresponding viability maps used in this study is deposited in the GitHub repository “shenghh2015/label-free-viability-assay” [<https://github.com/shenghh2015/label-free-viability-assay>]. The complete dataset is not deposited due to its massive size, but is available from the corresponding author upon request. Requests will be answered within two weeks. Source data are provided with this paper.

## Code availability

The MATLAB script to generate semantic segmentation maps, along with representative input images is provided as Supplementary Software. The trained E-U-Net models along with sample testing images are available for download at <https://github.com/shenghh2020/label-free-viability-assay>.

Received: 29 March 2021; Accepted: 11 January 2022;

Published online: 07 February 2022

## References

- Riss, T. L. et al. Cell viability assays, in *Assay Guidance Manual [Internet]*. Eli Lilly & Company and the National Center for Advancing Translational Sciences (2016).
- Strober, W. Trypan blue exclusion test of cell viability. *Curr. Protoc. Immunol.*, 2001. Appendix 3: p. Appendix 3B (2001).
- Phillips, H. J. Dye exclusion tests for cell viability. in *Tissue culture* 406–408 (1973).
- van Meerloo, J., Kaspers, G. J. & Cloos, J. Cell sensitivity assays: the MTT assay. *Methods Mol. Biol.* **731**, 237–245 (2011).
- Ciapetti, G. et al. In vitro evaluation of cell/biomaterial interaction by MTT assay. *Biomaterials* **14**, 359–364 (1993).
- Kumar, P., Nagarajan, A. & Uchil, P. D. Analysis of cell viability by the MTT assay. *Cold Spring Harb Protoc.* **2018** (2018).
- Altman, S. A., Randers, L. & Rao, G. Comparison of trypan blue dye exclusion and fluorometric assays for mammalian cell viability determinations. *Biotechnol. Prog.* **9**, 671–674 (1993).
- Breeuwer, P. & Abee, T. Assessment of viability of microorganisms employing fluorescence techniques. *Int J. Food Microbiol.* **55**, 193–200 (2000).
- Haugland, R. P., MacCoubrey, I. C. & Moore, P. L. Dual-fluorescence cell viability assay using ethidium homodimer and calcein AM. Google Patents (1994).
- Millard, P. J. et al. Fluorescent viability assay using cyclic-substituted unsymmetrical cyanine dyes. Google Patents (1996).
- Park, Y., Depeursinge, C. & Popescu, G. Quantitative phase imaging in biomedicine. *Nat. Photonics* **12**, 578–589 (2018).
- Popescu, G. Quantitative phase imaging of cells and tissues. McGraw-Hill biophotonics. New York: McGraw-Hill. xx, 362 p (2011).
- Hu, C. et al. Optical excitation and detection of neuronal activity. *J Biophoton.* **12**, e201800269 (2018).
- Kandel, M. E. et al. Epi-illumination gradient light interference microscopy for imaging opaque structures. *Nat. Commun.* **10**, 4691 (2019).
- Merola, F. et al. Tomographic flow cytometry by digital holography. *Light Sci. Appl.* **6**, e16241 (2017).
- Lee, K. et al. Quantitative phase imaging techniques for the study of cell pathophysiology: from principles to applications. *Sens. (Basel)* **13**, 4170–4191 (2013).
- Kim, K. et al. Real-time visualization of 3-D dynamic microscopic objects using optical diffraction tomography. *Opt. Express* **21**, 32269–32278 (2013).
- Chen, X. et al. Wolf phase tomography (WPT) of transparent structures using partially coherent illumination. *Light Sci. Appl.* **9**, 142 (2020).
- Eldridge, W. J. et al. Optical phase measurements of disorder strength link microstructure to cell stiffness. *Biophys. J.* **112**, 692–702 (2017).
- Popescu, G. et al. Optical measurement of cell membrane tension. *Phys. Rev. Lett.* **97**, 218101 (2006).
- Hu, C. et al. Imaging collagen properties in the uterosacral ligaments of women with pelvic organ prolapse using spatial light interference microscopy (SLIM). *Front. Phys.* **7**, 72 (2019).
- Kim, B. S. et al. Electrothermal soft manipulator enabling safe transport and handling of thin cell/tissue sheets and bioelectronic devices. *Sci. Adv.* **6**, eabc5630 (2020).

23. Christiansen, E. M. et al. In silico labeling: predicting fluorescent labels in unlabeled images. *Cell* **173**, 792–803. e19 (2018).
24. Ounkomol, C. et al. Label-free prediction of three-dimensional fluorescence images from transmitted-light microscopy. *Nat. Methods* **15**, 917–920 (2018).
25. Liu, R. R. et al. Deep spectral learning for label-free optical imaging oximetry with uncertainty quantification. *Light-Sci. Appl.* **8**, 102 (2019).
26. Kandel, M. E. et al. Phase imaging with computational specificity (PICS) for measuring dry mass changes in sub-cellular compartments. *Nat. Commun.* **11**, 6256 (2020).
27. Rivenson, Y., Wu, Y. & Ozcan, A. Deep learning in holography and coherent imaging. *Light Sci. Appl.* **8**, 85 (2019).
28. Rivenson, Y. et al. Phase recovery and holographic image reconstruction using deep learning in neural networks. *Light-Sci. Appl.* **7**, 17141 (2018).
29. Bostan, E. et al. Deep phase decoder: self-calibrating phase microscopy with an untrained deep neural network. *Optica* **7**, 559–562 (2020).
30. Wu, Z. H. et al. SIMBA: scalable inversion in optical tomography using deep denoising priors. *IEEE J. Sel. Top. Signal Process.* **14**, 1163–1175 (2020).
31. Rivenson, Y. et al. PhaseStain: the digital staining of label-free quantitative phase microscopy images using deep learning. *Light Sci. Appl.* **8**, 23 (2019).
32. Nygate, Y. N. et al. Holographic virtual staining of individual biological cells. *Proc. Natl Acad. Sci. USA* **117**, 9223–9231 (2020).
33. Jo, Y. et al. Quantitative phase imaging and artificial intelligence: a review. *IEEE J. Selected Top. Quant. Electron.* **25**, 1–14 (2019).
34. Kandel, M. E. et al. Reproductive outcomes predicted by phase imaging with computational specificity of spermatozoon ultrastructure. *Proc. Natl Acad. Sci. USA* **117**, 18302–18309 (2020).
35. Wang, Z. et al. Spatial light interference microscopy (SLIM). *Opt. Express* **19**, 1016–1026 (2011).
36. Kim, T. et al. White-light diffraction tomography of unlabelled live cells. *Nat. Photon* **8**, 256–263 (2014).
37. Tan, M. & Le, Q. V. Efficientnet: rethinking model scaling for convolutional neural networks. arXiv preprint arXiv:1905.11946, (2019).
38. Pan, S. J. & Yang, Q. A survey on transfer learning. *IEEE Transactions on knowledge and data engineering.* **22** 1345–1359 (2010).
39. Hu, C. & Popescu, G. Quantitative phase imaging: principles and applications, in *Label-Free Super-Resolution Microscopy*. pp. 1–24 (Springer, 2019).
40. Hu, C. & Popescu, G. Quantitative phase imaging (QPI) in neuroscience. *IEEE J. Sel. Top. Quantum Electron.* **25**, 1–9 (2019).
41. Miller, M. A. & Zachary, J. F. Mechanisms and morphology of cellular injury, adaptation, and death. *Pathologic Basis Veterinary Dis.* 2–43.e19 (2017).
42. Deng, J. et al. ImageNet: a large-scale hierarchical image database. *Cvpr: 2009 IEEE Conference on Computer Vision and Pattern Recognition*, Vols 1–4, 248–255 (2009).
43. Kingma, D. P. & Ba, J. *Adam: A method for stochastic optimization*. arXiv preprint arXiv:1412.6980, (2014).
44. Caicedo, J. C. et al. Evaluation of deep learning strategies for nucleus segmentation in fluorescence images. *Cytom. A* **95**, 952–965 (2019).
45. Eldridge, W. J., Hoballah, J. & Wax, A. Molecular and biophysical analysis of apoptosis using a combined quantitative phase imaging and fluorescence resonance energy transfer microscope. *J. Biophoton.* **11**, e201800126 (2018).
46. Pavillon, N. et al. Early cell death detection with digital holographic microscopy. *PLoS ONE* **7**, e30912 (2012).
47. Vicar, T. et al. The quantitative-phase dynamics of apoptosis and lytic cell death. *Sci. Rep.* **10**, 1566 (2020).
48. Tinevez, J. Y. et al. TrackMate: an open and extensible platform for single-particle tracking. *Methods* **115**, 80–90 (2017).
49. Duprez, L. et al. Major cell death pathways at a glance. *Microbes Infect.* **11**, 1050–1062 (2009).
50. Krysko, D. V. et al. Apoptosis and necrosis: detection, discrimination and phagocytosis. *Methods* **44**, 205–221 (2008).
51. Rommel, C. E. et al. Multimodal label-free in vitro toxicity testing with digital holographic microscopy. *Biophotonics: Photonic Solutions for Better Health Care Iv* **9129**, 912940 (2014).
52. Kim, Y. S. et al. Combining three-dimensional quantitative phase imaging and fluorescence microscopy for the study of cell pathophysiology. *Yale J. Biol. Med.* **91**, 267–277 (2018).
53. Chowdhury, S. et al. Spatial frequency-domain multiplexed microscopy for simultaneous, single-camera, one-shot, fluorescent, and quantitative-phase imaging. *Opt. Lett.* **40**, 4839–4842 (2015).
54. Dubey, V. et al. Multi-modal chip-based fluorescence and quantitative phase microscopy for studying inflammation in macrophages. *Opt. Express* **26**, 19864–19876 (2018).
55. Kumar, M. et al. Digital holographic multimodal cross-sectional fluorescence and quantitative phase imaging system. *Sci. Rep.* **10**, 7580 (2020).
56. Avalos Vizcarra, I. et al. Fluorescence-based in situ assay to probe the viability and growth kinetics of surface-adhering and suspended recombinant bacteria. *Biointerphases* **8**, 22 (2013).
57. Verrier, S. et al. In situ monitoring of cell death using Raman microspectroscopy. *Biopolymers* **74**, 157–162 (2004).
58. Miklaszewski, A. et al. Nanoscale size effect in in situ titanium based composites with cell viability and cytocompatibility studies. *Mater. Sci. Eng. C* **73**, 525–536 (2017).
59. Mueller, D. et al. Real-time in situ viability assessment in a 3D bioreactor with liver cells using resazurin assay. *Cytotechnology* **65**, 297–305 (2013).
60. Zhang, D. et al. Bond-selective transient phase imaging via sensing of the infrared photothermal effect. *Light Sci. Appl.* **8**, 116 (2019).
61. Hu, C. F. et al. Harmonic optical tomography of nonlinear structures. *Nat. Photonics* **14**, 564 (2020).
62. Lin, T. Y. et al. Focal loss for dense object detection. *IEEE Trans. Pattern Anal. Mach. Intell.* **42**, 318–327 (2020).
63. Milletari, F. et al. Fully convolutional neural networks for volumetric medical image segmentation. in *Proceedings of the 2016 Fourth International Conference on 3D Vision (3DV)*.

## Acknowledgements

National Science Foundation (0939511, 1353368), G.P. National Institute of Health (R01CA238191, R01GM129709), G.P. National Institute of Health – Tissue Micro-environment (TiMe) training program (T32EB019944), C.H.

## Author contributions

G.P. and C.H. conceived the idea. C.H. designed the experiment, collected data, generated semantic segmentation maps, performed deep learning testing, and conducted data analysis. S.H. led the deep learning training and validation. Y.L. prepared cell cultures. Y.H. performed software integration. E.M.K prepared the script for PICS evaluation. C.H. and S.H. wrote the manuscript with input from all authors. M.A.A. and H.L. supervised the deep learning. G.P. supervised the project.

## Competing interests

G.P. has financial interest in Phi Optics, a company developing quantitative phase imaging technology for materials and life science applications, which, however, did not sponsor the research. C.H., S.H., Y.H., M.A., and G.P. have disclosed the invention to the Office of Technology Management at the University of Illinois at Urbana-Champaign for patent applications. The remaining authors declare no competing interests.

## Additional information

**Supplementary information** The online version contains supplementary material available at <https://doi.org/10.1038/s41467-022-28214-x>.

**Correspondence** and requests for materials should be addressed to Mark A. Anastasio or Gabriel Popescu.

**Peer review information** *Nature Communications* thanks Jan Balvan and the other, anonymous, reviewer(s) for their contribution to the peer review of this work. Peer reviewer reports are available.

**Reprints and permission information** is available at <http://www.nature.com/reprints>

**Publisher's note** Springer Nature remains neutral with regard to jurisdictional claims in published maps and institutional affiliations.



**Open Access** This article is licensed under a Creative Commons Attribution 4.0 International License, which permits use, sharing, adaptation, distribution and reproduction in any medium or format, as long as you give appropriate credit to the original author(s) and the source, provide a link to the Creative Commons license, and indicate if changes were made. The images or other third party material in this article are included in the article's Creative Commons license, unless indicated otherwise in a credit line to the material. If material is not included in the article's Creative Commons license and your intended use is not permitted by statutory regulation or exceeds the permitted use, you will need to obtain permission directly from the copyright holder. To view a copy of this license, visit <http://creativecommons.org/licenses/by/4.0/>.

© The Author(s) 2022

Supplemental Information for

**Live-dead assay on unlabeled cells using phase imaging with computational specificity**

*Chenfei Hu, Shenghua He, Young Jae Lee, Yuchen He, Edward M. Kong, Hua Li*

*Mark A. Anastasio, and Gabriel Popescu*

**Supplementary Note 1: Semantic map generation**

Semantic segmentation maps were generated in MATLAB with a customized script. First, for each NucBlue and NucGreen image pair, an adaptive thresholding was applied to separate the cell nucleus and background, where the segmented cell nuclei were obtained by computing the union of the binarized fluorescent image pair. We removed the segmentation artifacts by filtering out the tiny objects below the size of a typical nucleus. Next, using on the segmentation masks, we calculated the ratio between the NucGreen and NucBlue fluorescence signal. A histogram of the average ratio within the cell nucleus is plotted in Fig. S1, where three distinctive peaks were observed corresponding to the live, injured and dead cells. Because NucGreen/NucBlue reagent is only designed for live and dead classification, the histogram of injured cells is partially overlapped with the live cells. By selecting a threshold value that gives the lowest histogram count between dead and injured cells, we assigned label “live” to all live and injured cells, while the remaining cells as “dead”.

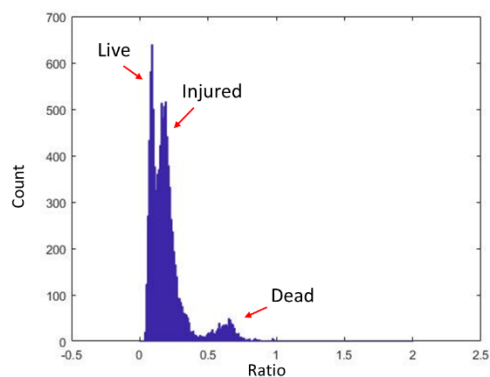


Figure S1. Histogram of fluorescence signal ratio.

### Supplementary Note 2: EfficientNet

The MBConvX is the principal module in an EfficientNet. It approximately factorizes a standard convolutional layer into a sequence of separable layers to shrink the number of parameters needed in a convolution operation while maintaining a comparable ability of feature extraction. The separable layers in a MBConvX module are shown in Fig. 2c. Here, MBConv1(X=1) and MBConv6 (X=6) indicate that a ReLU layer and ReLU6 layer are employed in this module, respectively. ReLU6 is a modification of the rectified linear unit, where the activation is limited to a maximum size of 6. A MBConvX module in Fig. 2b may include a down-sampling layer, which can be inferred by the indicated feature map dimensions. The first MBConvX in each layer block does not contain a skip connection between its input and output (indicated as a dash line in Fig. 2c), since the input and output of that module have different sizes.

### Supplementary Note 3: PICS evaluation at a cellular level

We implemented a U-Net based EfficientNet (E-U-Net) to extract markers associated with viable state of cells measured by SLIM. In Table S1, we show the conventional confusion matrix and corresponding F1 score evaluated on pixels in testing images. Figure S2a shows a represented raw E-U-Net output image. As indicated by the yellow arrow, there exist cases where a segmented cell may have multiple semantic labels. The conventional deep learning evaluation method only focuses on assessing pixel-wise segmentation accuracy, which overlooks some biologically relevant instances (the viable state of the entire cell) [1]. And this motivates us to adopt an object-based evaluation that estimates the E-U-Net accuracy for individual cell.

<b>Actual Prediction</b>	<b>Live</b>	<b>Dead</b>	<b>Background</b>
<b>Live</b>	3699117	2591	1068559
<b>Dead</b>	1422	221396	187715
<b>Background</b>	696478	44028	62668870
<b>F1 Score</b>	80.7%	65.3%	98.4%

Table S1. **Pixel-wise evaluation of the trained E-U-Net.** Due to the fact that the E-U-Net prediction assigns multiple labels to one cell nucleus, we converted the pixel-wise classification into cell-wise classification, which is more relevant biologically (Table 1 in the main text).

First, we use dominant semantic label across a cellular region to denote the viable state for this cell (Figure S2b). And we compare this semantic label with the same cell in ground truth image, repeat this step across all testing images, and obtain the cell-wise evaluation as shown in the article Table 1.

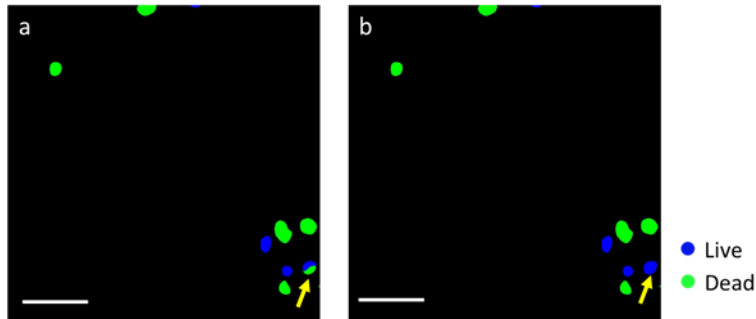


Figure S2. **a.** Output of E-U-Net on a representative testing image. The network assigns semantic labels to each pixel, and thus for some cells, more than one semantic label can be observed within the cell body. **b.** we use the dominant semantic label to indicate the viability state of a cell, and then the performance of training is evaluated at a cellular level, referred to the cell-wise evaluation. The images are randomly selected from a combined dataset across 4 imaging experiments. Scale bars: 50  $\mu\text{m}$  in space.

#### **Supplementary Note 4: PICS on CHO cells**

##### **Evaluate the effect of lytic cell death**

Before performing experiments on CHO cells, a preliminary study was conducted, as follows. We prepared live cell cultures and split them into the two groups. 1  $\mu\text{M}$  of staurosporine was added into the medium of the experimental group, whereas the others were kept intact as control. Both control and experimental cells were measured with SLIM for 10 hours under regular incubation condition (37  $^{\circ}\text{C}$  and 5% concentration of  $\text{CO}_2$ ). Figure S3a and S3b show the QPI images of experimental and control cells measured at  $t = 0.5, 6.5, 7$  and 10 hours, respectively. Throughout the time-course, the untreated cells remained attached to the petri-dish. Moreover, as indicated by the yellow arrows, the control cells divided at  $t = 6.5$  hr. In contrast, cells treated with staurosporine

presented drastically different characteristics, where the cell volume decreased, and membrane ruptured or became detached. This preliminary result suggests that, under our regular incubation condition, the cells did not suffer from lytic cell death.

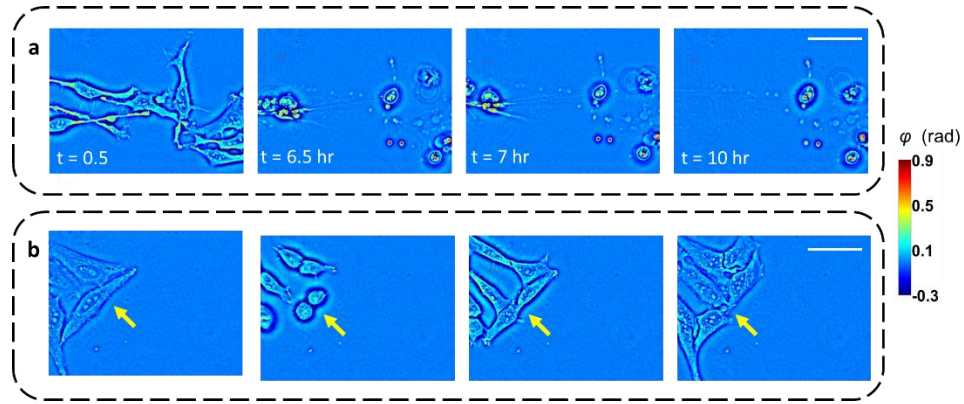


Figure S3. Time-lapse SLIM recording of CHO cells with (a) and without (b) staurosporine that introduces cell apoptosis, under regular incubation condition. For the control group, the cells continued growing and dividing without signs of cell death, which ruled out the existence of lytic cell death. The images are selected from 1 experiments, and the results are consistent across 27 measured field of views (FOV). Scale bar: 50  $\mu\text{m}$  in space

### PICS training and testing on CHO cell images

After validation the efficacy of staurosporine on introducing apoptotic cell death, we acquired images on CHO cells and generated the dataset for PICS training. The training was conducted on E-U-Net (EfficientNet-B7), whose network architecture, and its training/validation loss are shown in Figure. S4.

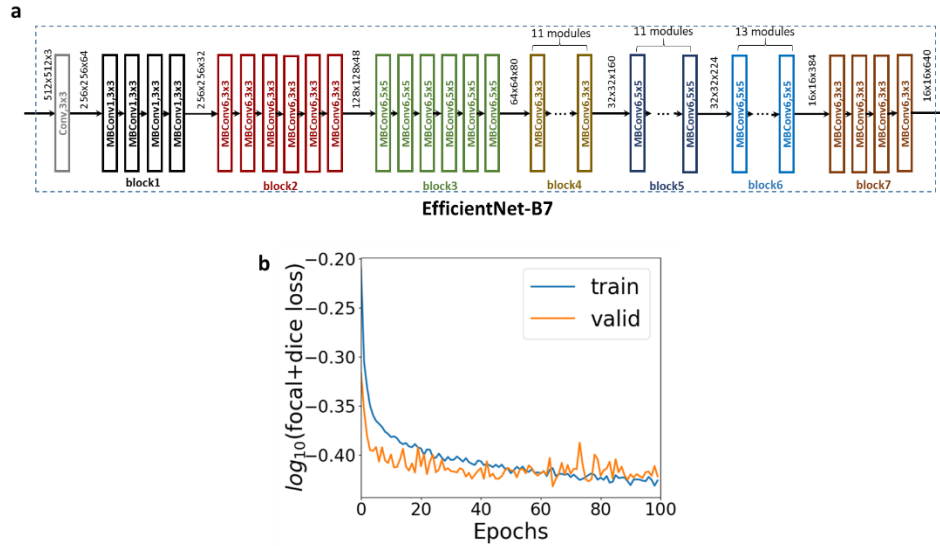


Figure S4. **CHO cells viability training with EfficientNet-B7.** **a.** The network architecture of EfficientNet-B7. **b.** Training and validation focal losses vs number of epochs plotted in the log scale.

We visually inspected the difference between the ground truth and machine learning prediction in the testing dataset. First, we saw prediction errors due to cells located at the boundary of the FOV, as explained in the previous comments. In addition, we found rare cases where live CHO cells were mistakenly labeled as dead (see Fig. S5 below for an illustration of CHO cells with staurosporine administration at  $t = 0.5$  hour). In SLIM, these cells present features of abnormal cell shapes and decreased phase values, but severe membrane rupture was not observed. Previous studies suggested that these morphological features are early indicators of cell death [2-4], but it was identified as live using traditional fluorometric evaluation.

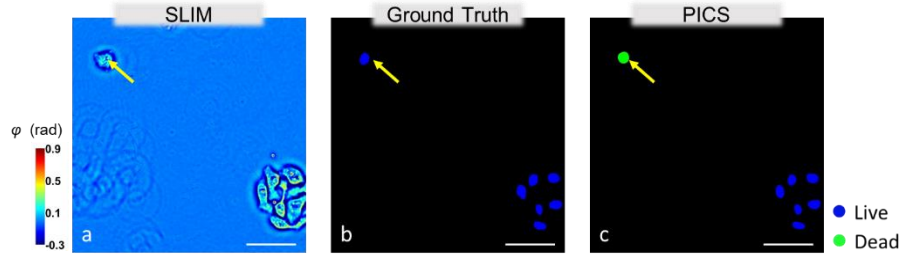


Figure S5. Cells with irregular shapes but no severe membrane rupture are subjected to erroneous classification. **a.** Input SLIM image. **b.** Ground truth. **c.** PICS output based on input in **a.** The images are randomly selected from a combined dataset across 4 imaging experiments. Scale bar: 50  $\mu\text{m}$  in space

### PICS performance on cells under different confluence

As discussed in the manuscript, live CHO cell culture was prepared in a 6-well plate at three confluence levels, staurosporine solution was added into the culture medium to introduce apoptosis. Figure. S6 show SLIM image of high, intermediate, and low confluence CHO cells measured at  $t = 0$ . Although, aggregating into clusters, the cell shape and boundary can be easily identified. All SLIM images were combined for training and validation. In testing, we estimated the PICS performance vs. cell confluence, and the results are summarized in Table. S2a-c.

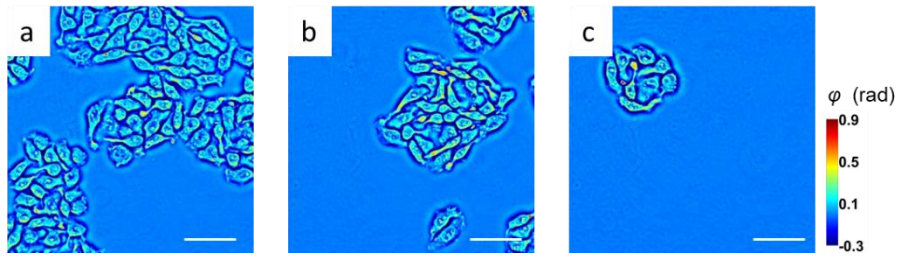


Figure S6. SLIM images of high (a), intermediate (b), and low (c) confluence CHO cells. The images are randomly selected from a combined dataset across 4 imaging experiments. Scale bar: 50  $\mu\text{m}$  in space

a	High	Live	Dead
	<b>Precision</b>	90.5%	98.5%
	<b>Recall</b>	94.7%	97.2%
	<b>F1 Score</b>	92.6%	97.8%

b	Intermediate	Live	Dead
	<b>Precision</b>	87.5%	98.7%
	<b>Recall</b>	96.3%	95.2%
	<b>F1 Score</b>	91.7%	96.9%

c	Low	Live	Dead
	<b>Precision</b>	96.2%	97.1%
	<b>Recall</b>	90.1%	98.9%
	<b>F1 Score</b>	93.1%	97.9%

Table S2. PICS performance vs. CHO cell confluence

### Training on unlabeled cell SLIM images

During the data acquisition, we added FL viability reagents at the beginning, and this allows us to monitor the viable state changes of the individual cells over time. However, such data

acquisition strategy can, in principle, introduce bias when optimizing the E-U-Net. This effect can be ruled out by collecting label-free images first, followed by exogenous staining and fluorescent imaging to obtain the ground truth, at the cost of increased efforts in staining, selecting FOV and re-focusing.

To study this potential effect, we performed a control experiment described as follows. Live CHO cells were prepared and passaged onto two glass-bottom 6-well plates. 1  $\mu$ M of staurosporine was added into each well to introduce apoptosis. At  $t = 0$ , cells in one well were imaged by SLIM, followed by reagents staining and fluorescence imaging. After 60 minutes, we repeated this step, but measuring the cells in the other well. Throughout the experiment, the cells were maintained in 37 °C and 5% concentration of CO<sub>2</sub>. In this way, cells in each well were only measured once, and we obtained a dataset of unlabeled QPI images that resemble the structure of a testing dataset used in this study. The experiment was repeated 4 times, resulting in a total of 2400 SLIM and fluorescent pairs, on which PICS training and testing were performed. Table S3 shows the PICS performance on this new dataset, where live and dead cells were classified with 99% and 97% sensitivity, respectively. Thus, we can conclude that PICS optimization on cells without fluorescent stains does not compromise the prediction accuracy, which makes the proposed live-dead assay method robust for a variety of experiment settings.

<b>Actual</b>	<b>Live (n= 2707)</b>	<b>Dead (n = 101)</b>
<b>Prediction</b>		
<b>Live</b>	98.9%	3.5%
<b>Dead</b>	1.1%	96.5%
<b>Precision</b>	99.8%	78.6%
<b>Recall</b>	98.9%	96.5%
<b>F1 Score</b>	99.3%	86.6%

Table S3. Evaluation of the PICS performance on truly unlabeled CHO cells with apoptosis reagents.

#### **Supplementary Note 5: Comparison of PICS performance under various training strategies**

We have attempted to compare cell viability prediction performance under various network architecture settings. We compared three network settings: 1) an E-U-net trained by use of a pre-trained EfficientNet; 2) an E-U-net trained from scratch; and 3) a standard U-net [5] trained from scratch. In these additional experiments, the U-net architecture employed was a standard U-net [5], with the exception that batch normalization layers were placed after each convolutional layer to facilitate the network training. EfficientNet-B0 was employed in the E-U-nets to make sure that the network size of E-U-net (7.8 million of parameters) approximately matched that of a standard U-net (7.85 million of parameters). A combined loss that comprised focal and dice losses (denoted as dice+focal loss) was used for network training. Other training settings were consistent with how the E-U-net was trained, as described in the manuscript. After the networks were trained with training and validation data from HeLa cell datasets and CHO cell datasets, they were tested on

the testing data from the two datasets, respectively. The average pixel-wise F1 scores over the live, dead and background classes were computed to evaluate the performance of the trained networks, as reported in Table S4. It can be observed from the table that, on both the two testing datasets, the average F1 scores corresponding to an E-U-net are much higher than those corresponding to a standard U-net when both of them were trained from scratch. Furthermore, as expected, an E-U-net trained with a pre-trained EfficientNet achieves a better performance than the one trained from scratch. These results demonstrate the effectiveness of the E-U-net architecture and the transfer learning techniques in training a deep neural network for pixel-wise cell viability prediction.

<b>Network</b>	<b>E-U-Net (pre-trained)</b>	<b>E-U-Net (scratch)</b>	<b>Standard U-Net (scratch)</b>
<b>HeLa</b>	80.6%	75.0%	72.0%
<b>CHO</b>	85.7%	80.4%	76.0

Table S4. Average F1 scores related to E-U-nets trained with a pre-trained EfficientNet-B0, E-U-nets trained from scratch, and standard U-nets trained from scratch, respectively.

In addition, we compared the average pixel-wise F1 scores corresponding to E-U-nets trained with various loss functions, including a dice+focal loss, a standard focal loss, a standard dice loss, and a weighted cross entropy (WCE) loss. To be consistent with the network settings in the manuscript, a pre-trained EfficientNet-B3 and a pre-trained EfficientNet-B7 were employed for training the E-U-nets on the HeLa cell dataset and CHO cell datasets, respectively. The class weights related to live, dead, and background classes in the weighted cross entropy loss were set to [0.17, 2.82, 0.012] and [2.32, 0.654, 0.027] for the network training on the HeLa cell dataset and CHO cell datasets, respectively. In each of the weight cross entropy losses, the average of weights over the three classes is 1, and the weights related to each class were inversely proportional

to the percentages of pixels from each class in the HeLa cell and CHO cell training datasets: [6.7%, 0.4%, 92.9%] and [1.1%, 3.9%, 95%], respectively. Other network training settings were consistent with how the E-U-net was trained as described in the manuscript. The trained networks were then evaluated on the testing HeLa cell dataset containing 100 images and testing CHO cell dataset containing 288 images, respectively. The average pixel-wise F1 scores were computed over all pixels in the two testing sets as shown in Table S5. It can be observed in the table that, on both the two datasets, E-U-nets trained with a dice+focal loss produced higher average pixel-wise F1 scores than those trained with a dice loss or a WCE loss.

<b>Loss</b>	<b>Dice + focal</b>	<b>Focal</b>	<b>Dice</b>	<b>WCE</b>
<b>HeLa</b>	81.2%	81.4%	80.8%	79.4
<b>CHO</b>	88.0%	87.4%	87.0%	85.2%

Table S5. Average F1 scores related to E-U-nets trained with various loss functions.

We further compared E-U-nets trained with a dice+focal loss to those trained with a dice loss or a WCE loss by investigating their agreements on the dice coefficients of each class related to the predictions for each image sample in the two testing datasets. Here, let us denote  $D_{\text{dice+focal}}$ ,  $D_{\text{dice}}$ , and  $D_{\text{WCE}}$  as the dice coefficients produced by E-U-nets trained with a dice+focal loss, a dice loss and a weighted cross entropy loss, respectively. Bland-Altman plots were employed to analyze the agreement between  $D_{\text{dice+focal}}$  and  $D_{\text{dice}}$  and that between  $D_{\text{dice+focal}}$  and  $D_{\text{WCE}}$  on testing dataset of HeLa and that of CHO, respectively. Here, a Bland-Altman plot of two paired dice coefficients (i.e.  $D_{\text{dice+focal}}$  vs.  $D_{\text{dice}}$ ) produces a scatter plot  $x$ - $y$ , in which the  $y$  axis (vertical axis) represents the difference between the two paired dice coefficients (i.e.  $D_{\text{dice+focal}} - D_{\text{dice}}$ ) and the  $x$  axis (horizontal

axis) shows the average of the two dice coefficients (i.e.  $(D_{\text{dice+focal}} + D_{\text{dice}})/2$ ).  $\mu_d$  and  $\sigma_d$  represent the mean and standard deviation of the differences of the paired dice coefficients over the image samples in a specific testing dataset. The results corresponding to  $D_{\text{dice+focal}}$  vs.  $D_{\text{dice}}$  and  $D_{\text{dice+focal}}$  vs.  $D_{\text{WCE}}$  are reported in Figure S7 and Figure S8, respectively. In each figure, the subplots from left to right show the Bland-Altman plots related to the predictions for live, dead, and background classes, respectively. It can be observed from Figures S7-8 that, for predicting live and dead pixels, both the  $D_{\text{dice+focal}} > D_{\text{dice}}$  (or  $D_{\text{dice+focal}} - D_{\text{dice}} > 0$ ) and  $D_{\text{dice+focal}} > D_{\text{WCE}}$  (or  $D_{\text{dice+focal}} - D_{\text{WCE}} > 0$ ) hold at the majority of the image samples in the two datasets, though for the background prediction,  $D_{\text{dice+focal}}$  is comparable to  $D_{\text{dice}}$  and  $D_{\text{WCE}}$ . These results suggest that compared to a dice or WCE loss, a focal+dice loss can improve the performance of predicting live and dead pixels for the majority of testing images from both the two datasets.

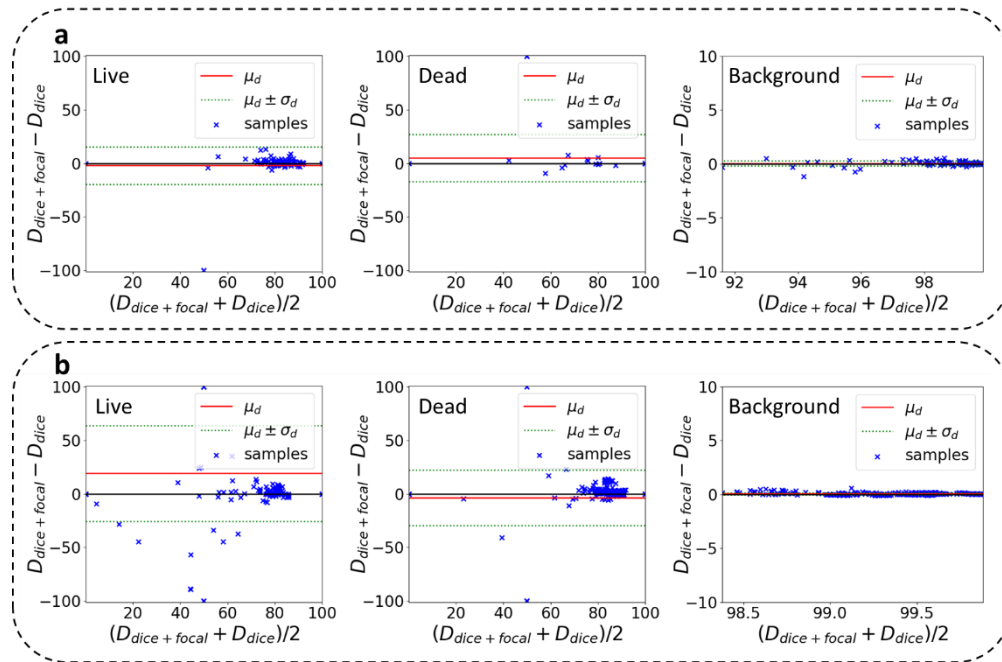


Figure S7.  $D_{\text{dice+focal}}$  vs.  $D_{\text{dice}}$  on testing dataset of HeLa (a) and CHO (b), where  $\mu_d$  and  $\sigma_d$  represent the mean and standard deviation of  $D_{\text{dice+focal}} - D_{\text{dice}}$ .

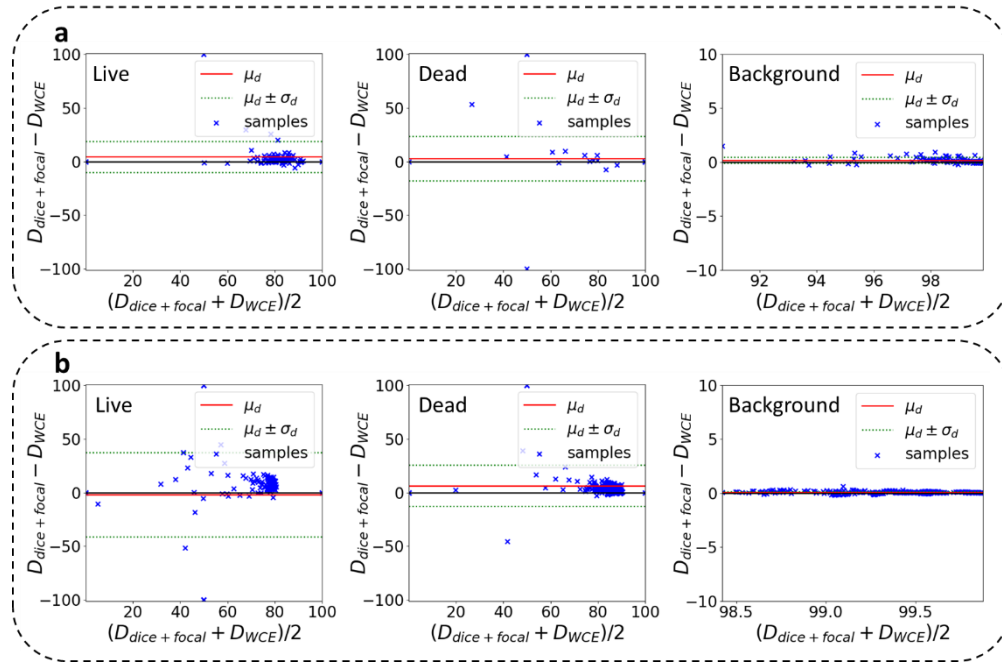


Figure S8.  $D_{\text{dice+focal}}$  vs.  $D_{\text{WCE}}$  on testing dataset of HeLa (a) and CHO (b), where  $\mu_d$  and  $\sigma_d$  represent the mean and standard deviation of  $D_{\text{dice+focal}} - D_{\text{WCE}}$ .

## References:

1. Caicedo, J.C., et al., *Evaluation of Deep Learning Strategies for Nucleus Segmentation in Fluorescence Images*. Cytometry A, 2019. **95**(9): p. 952-965.
2. Eldridge, W.J., J. Hoballah, and A. Wax, *Molecular and biophysical analysis of apoptosis using a combined quantitative phase imaging and fluorescence resonance energy transfer microscope*. Journal of Biophotonics, 2018. **11**(12): p. e201800126.
3. Pavillon, N., et al., *Early cell death detection with digital holographic microscopy*. PLoS One, 2012. **7**(1): p. e30912.
4. Vicar, T., et al., *The Quantitative-Phase Dynamics of Apoptosis and Lytic Cell Death*. Scientific Reports, 2020. **10**(1).
5. Ronneberger, O., P. Fischer, and T. Brox, *U-Net: Convolutional networks for biomedical image segmentation*. arXiv 2015. arXiv preprint arXiv:1505.04597, 2019.